Ray-tracing simulations of coupled dark energy models

Francesco Pace,[1]⋆ Marco Baldi,[2,3,4] Lauro Moscardini,[2,3,4] David Bacon[1] and Robert Crittenden[1]

[1]*Institute of Cosmology and Gravitation, University of Portsmouth, Dennis Sciama Building, Portsmouth PO1 3FX, UK*
[2]*Dipartimento di Fisica e Astronomia, Università di Bologna, Viale Berti Pichat 6/2, I-40127 Bologna, Italy*
[3]*INFN, Sezione di Bologna, Viale Berti Pichat 6/2, I-40127 Bologna, Italy*
[4]*INAF, Osservatorio Astronomico di Bologna, Via Ranzani 1, I-40127 Bologna, Italy*

ABSTRACT

Dark matter and dark energy are usually assumed to couple only gravitationally. An extension to this picture is to model dark energy as a scalar field coupled directly to cold dark matter. This coupling leads to new physical effects, such as a fifth force and a time-dependent dark matter particle mass. In this work we examine the impact that coupling has on weak lensing statistics by constructing realistic simulated weak lensing maps using ray-tracing techniques through *N*-body cosmological simulations. We construct maps for different lensing quantities, covering a range of scales from a few arcminutes to several degrees. The concordance Λ cold dark matter (ΛCDM) model is compared to different coupled dark energy models, described either by an exponential scalar field potential (standard coupled dark energy scenario) or by a SUGRA potential (bouncing model). We analyse several statistical quantities and our results, with sources at low redshifts are largely consistent with previous work on cosmic microwave background lensing by Carbone et al. The most significant differences from the ΛCDM model are due to the enhanced growth of the perturbations and to the effective friction term in non-linear dynamics. For the most extreme models, we see differences in the power spectra up to 40 per cent compared to the ΛCDM model. The different time evolution of the linear matter overdensity can account for most of the differences, but when controlling for this using a ΛCDM model having the same normalization, the overall signal is smaller due to the effect of the friction term appearing in the equation of motion for dark matter particles.

Key words: gravitational lensing: weak – methods: numerical – cosmological parameters – cosmology: theory – dark energy – large-scale structure of Universe.

1 INTRODUCTION

A wealth of cosmological probes have confirmed the accelerated expansion of the Universe first inferred with observations of Type Ia supernovae (SNe; Riess et al. 1998, 2004; Schmidt et al. 1998; Perlmutter et al. 1999; Astier et al. 2006; Kowalski et al. 2008; Kessler et al. 2009; Conley et al. 2011; Sullivan et al. 2011). These include the angular power spectrum of the cosmic microwave background (CMB) fluctuations and the integrated Sachs–Wolfe effect (Jaffe et al. 2001; Giannantonio et al. 2008; Ho et al. 2008; Jarosik et al. 2011; Komatsu et al. 2011; Sherwin et al. 2011; Hinshaw et al. 2013; Planck Collaboration XV 2014a; Planck Collaboration XVI 2014b; Planck Collaboration XIX 2014c), the number counts of massive galaxy clusters (Haiman, Mohr & Holder 2001; Allen et al. 2004, 2008; Wang et al. 2004; Vikhlinin et al. 2009; Mantz

et al. 2010; Rapetti et al. 2010; Rozo et al. 2010; Benson et al. 2013), weak lensing (Hoekstra et al. 2006; Jarvis et al. 2006; Fu et al. 2008; Schrabback et al. 2010; Kilbinger et al. 2013), galaxy clustering (Percival et al. 2001; Tegmark et al. 2004; Cole et al. 2005; Guzzo et al. 2008; Reid et al. 2010; Blake et al. 2012; de la Torre et al. 2013) and baryon acoustic oscillations (BAO; Eisenstein et al. 2005; Percival et al. 2010; Parkinson et al. 2012; Sánchez et al. 2014; Veropalumbo et al. 2014). To explain this acceleration, a new dark component with equation of state $w < -1/3$ has been introduced dubbed dark energy (DE). As with dark matter (DM), the DE also does not interact with the electromagnetic field (Bertone, Hooper & Silk 2005; Bartelmann 2010; Astier & Pain 2012, and references therein) and its nature is still completely unknown after more than a decade of theoretical and observational investigations.

Continuous improvements in observations have led to the definition of a standard model in cosmology; in the concordance cosmological model (CCM) the Universe is filled with baryons ($\simeq$ 5 per cent of the total energy budget), DM ($\simeq$ 27 per cent) and

⋆E-mail: francesco.pace@manchester.ac.uk

DE ($\simeq 68$ per cent; Planck Collaboration XVI 2014b). In its simplest form, the DE is assumed to be a cosmological constant, characterized by an equation of state ($w = -1$) and energy density constant throughout the whole cosmic history.

Despite its simplicity, the CCM fits virtually all the available observations (Planck Collaboration XVI 2014b, and references therein). Nevertheless, the cosmological constant suffers severe problems from a theoretical point of view. In particular the actual value of the cosmological constant requires an extreme fine-tuning, giving rise to the coincidence (Zlatev, Wang & Steinhardt 1999) and fine-tuning problems (Weinberg 1989; Sahni & Starobinsky 2000). This provides motivation to find viable alternatives to overcome these fundamental problems, for example considering dynamical DE models or modifications to gravity.

Moreover, despite the fact that the cosmological constant scenario can explain most observations at cosmological scales, many phenomena at small and intermediate scales indicate possible problems with this simple model. These include the lack of luminous satellites in cold dark matter (CDM) haloes (Navarro, Frenk & White 1996; Boylan-Kolchin, Bullock & Kaplinghat 2011), the observed low baryon fraction in galaxy clusters (Ettori 2003; McCarthy, Bower & Balogh 2007) and the high velocities detected in the large-scale bulk motion of galaxies (Watkins, Feldman & Hudson 2009). A simple explanation for these features may be related to the fact that our understanding of the baryonic physics at these scales is still very incomplete, but nevertheless it is worth investigating whether alternative models could accommodate or diminish the tension between these observations and theory.

One interesting direction is to study interactions in the dark sector between the DE and the DM component. Coupled dark energy (cDE) models were first introduced by Wetterich (1995) and Amendola (2000) in order to alleviate the fine-tuning problem; these have since been studied in some detail (Amendola 2004; Amendola, Campos & Rosenfeld 2007; Amendola, Baldi & Wetterich 2008; di Porto & Amendola 2008; Pettorino & Baccigalupi 2008; Caldera-Cabral, Maartens & Ureña-López 2009a; Caldera-Cabral, Maartens & Schaefer 2009b; Koyama, Maartens & Song 2009; Böhmer et al. 2010; Lopez Honorez et al. 2010; Majerotto, Väliviita & Maartens 2010; Väliviita, Maartens & Majerotto 2010; Baldi 2011a,b, 2012b; Clemson et al. 2012). Observational constraints on the interaction strength were obtained using the CMB (Bean et al. 2008; La Vacca et al. 2009; Xia 2009). These models have also been investigated using numerical simulations (Macciò et al. 2004; Baldi et al. 2010, 2011; Li 2011; Li & Barrow 2011a,b) which showed that significant deviations from the ΛCDM model have to be expected in the non-linear regime.

In this class of models the role of DE is played by a dynamical scalar field and there is a coupling describing an exchange of energy–momentum between DM and DE. While observations put strong constraints on the amount of interaction between the baryons and the dark sector (Hagiwara et al. 2002), this is not the case for interactions in the dark sector. A consequence of the coupling is the rise of a fifth force that modifies the equations of motion of DM and significantly affects the evolution of the collapsing structures. To account for this in the non-linear dynamics it is necessary to use expensive numerical simulations. In this work we make use of the largest available suite of such *N*-body simulations called Coupled Dark Energy Cosmological Simulation (CoDECS; Baldi 2012b). These simulations have been used to study the halo mass function (Cui, Baldi & Borgani 2012), the BAO (Cervantes et al. 2012), the galaxy rotation curves (Baldi & Salucci 2012), the redshift-space distortions (Marulli, Baldi & Moscardini 2012), the pairwise infall

velocity of colliding clusters (Lee & Baldi 2012) and the gravitational lensing effect (Beynon et al. 2012; Carbone et al. 2013).

Beynon et al. (2012) made predictions for the shear correlation function in the non-linear weak lensing regime based on CoDECS simulations of three 'standard' cDE models with an exponential potential and a reference ΛCDM model. This work utilized the analytical relation between the matter power spectrum and the shear correlation function: the shear power spectrum can be written as an integral along the line of sight of the (non-linear) matter power spectrum (Bartelmann & Schneider 2001). Taking the input matter power spectrum obtained directly from the particle distribution in the box, they derived predictions for the shear correlation; they also made forecasts for the Dark Energy Survey (DES)[1] and the *Euclid* mission[2] (Laureijs et al. 2011; Amendola et al. 2013) and showed that it will be possible to use lensing to distinguish between ΛCDM and cDE models at a 4σ level.

Carbone et al. (2013) instead performed a ray-tracing analysis, focusing on CMB lensing rather than lower redshift sources. Using the snapshots of the simulated box, the authors constructed deflection angle maps and studied the statistical properties of the deflection angle and lensing potential power spectrum. They analysed three different models: a reference ΛCDM model and two different cDE models, a standard scenario with an exponential potential and a bouncing model described by a SUGRA potential (Brax & Martin 1999). The authors showed that for the standard scenario, differences with the ΛCDM model arise from the interplay between an enhanced growth and a modified non-linear structure formation, while for the bouncing model these two effects make the power of the lensing signal ≈ 10 per cent smaller than for the reference ΛCDM model.

In this work, we extend both previous works (Beynon et al. 2012; Carbone et al. 2013) with a full numerical analysis of the statistical properties of several lensing quantities. In particular we analyse the superset of models studied in these two works from a completely numerical point of view, basing our work on ray-tracing simulations. An important goal of this work is to validate the semi-analytic method of Beynon et al. (2012) with a full numerical approach, and to check whether previous results are in agreement with a full non-linear treatment. Because of the different linear evolution in the coupled models, the perturbations have a different normalization of the matter power spectrum. In addition, the non-linear dynamics is different from the ΛCDM model, and effects induced by it might not be captured with the semi-analytical treatment. In order to separate the linear normalization differences from the differences in the non-linear physics, we also make a comparison with analytical models in the ΛCDM cosmology.

The paper is organized as follows. In Section 2 we briefly describe the main properties of the cDE cosmologies. The corresponding *N*-body simulations are described in Section 3. In Section 4.1 we describe the ray-tracing simulations. We present our results in Section 5. Finally, we conclude in Section 6.

2 COUPLED DARK ENERGY MODELS

In this work we consider weak gravitational lensing in the framework of cDE models. DE is represented by a classical scalar field ϕ that evolves in a self-interaction potential $V(\phi)$ and interacts directly with CDM particles by exchanging energy–momentum. This is due

---

[1] http://www.darkenergysurvey.org
[2] http://www.euclid-ec.org

to a source term at the level of the background continuity equations of the DE and CDM components, characterized by a coupling function $\beta(\phi)$.

More quantitatively, the background dynamics for radiation (subscript r), baryons (subscript b), CDM (subscript c) and DE scalar field (subscript ϕ) are, respectively, described by the following set of equations:

$$\dot{\rho}_r + 4H\rho_r = 0, \tag{1}$$

$$\dot{\rho}_b + 3H\rho_b = 0, \tag{2}$$

$$\dot{\rho}_c + 3H\rho_c = -\sqrt{\frac{2}{3}}\beta_c(\phi)\frac{\rho_c\dot{\phi}}{M_{Pl}}, \tag{3}$$

$$\ddot{\phi} + 3H\dot{\phi} + V'(\phi) = \sqrt{\frac{2}{3}}\beta_c(\phi)\frac{\rho_c}{M_{Pl}}, \tag{4}$$

where the Hubble function is given as usual by

$$H^2 = \frac{8\pi G}{3}\left(\rho_r + \rho_c + \rho_b + \rho_\phi\right), \tag{5}$$

and $M_{Pl}^2 \equiv 1/8\pi G$ is the reduced Planck mass. The scalar field ϕ is expressed in units of M_{Pl}, the overdot represents a derivative with respect to proper time and a prime stands for the derivative with respect to the scalar field.

The source terms in equations (3) and (4) define the interaction between the DM and the DE components. The coupling function $\beta_c(\phi)$ controls the strength of the interaction and the sign of the term $\dot{\phi}\beta_c(\phi)$ controls the direction of the energy–momentum flow between the two coupled components, with a positive sign implying the transfer of energy–momentum from CDM to DE. The presence of the coupling term implies that the mass of the DM particles is not constant any more, but changes in time according to the following equation:

$$\frac{d\ln(m_c/M_{Pl})}{dt} = -\sqrt{\frac{2}{3}}\beta_c\dot{\phi}. \tag{6}$$

The sign of $\dot{m}_c$ depends therefore on the sign of the flow: a positive (negative) value of $\dot{\phi}\beta_c(\phi)$ implies a decrement (increment) of the mass of DM particles. The equation of state of the DE component is given by $w_\phi \equiv P_\phi/\rho_\phi$, where the pressure P_ϕ and the density ρ_ϕ of the scalar field are defined as $P_\phi \equiv \dot{\phi}^2/2 - V(\phi)$ and $\rho_\phi \equiv \dot{\phi}^2/2 + V(\phi)$, respectively.

cDE models do not affect only the background expansion history of the universe, but also the evolution of matter density perturbations due to the appearance of a long-range fifth force term in the Euler equation. At the linear level, in the Newtonian limit and on subhorizon scales, the linear perturbed equations read (Amendola 2004; Pettorino & Baccigalupi 2008; Baldi 2011a)

$$\ddot{\delta}_c = -2H\left[1 - \beta_c\frac{\dot{\phi}}{\sqrt{6}H}\right]\dot{\delta}_c + 4\pi G[\bar{\rho}_b\delta_b + \bar{\rho}_c\delta_c\Gamma_c], \tag{7}$$

$$\ddot{\delta}_b = -2H\dot{\delta}_b + 4\pi G[\bar{\rho}_b\delta_b + \bar{\rho}_c\delta_c]. \tag{8}$$

In the previous equations, $\bar{\rho}_k$ represents the background density of the fluid k and $\delta_k \equiv \delta\rho_k/\bar{\rho}_k$ its density perturbation. Note the presence of the factor $\Gamma_c \equiv 1 + 4\beta_c^2/3$ due to the presence of the fifth force appearing only in the CDM equation. The term $\beta_c\dot{\phi}$ – also appearing only in the CDM equation – arises as a consequence of momentum conservation and effectively describes an additional friction term.

At the non-linear level, the acceleration experienced by DM particles is characterized by the two additional terms in the following equation:

$$\dot{\boldsymbol{v}}_c = \beta_c\frac{\dot{\phi}}{\sqrt{6}}\boldsymbol{v}_c - \nabla\left[\sum_c\frac{GM_c(\phi)\Gamma_c}{r_c} + \sum_b\frac{GM_b}{r_b}\right], \tag{9}$$

where $r_{c,b}$ are the physical distances of the target coupled particle from the other CDM and baryonic particles, respectively. Effects of the friction term have been studied in the literature (Amendola 2004; Baldi 2011a, 2012a).

3 THE CODECS SIMULATIONS

The basis for our lensing study is the suite of CODECS N-body simulations (Baldi 2012b). Here we briefly describe them and we refer to Baldi (2012b) for a more in-depth discussion.

The CODECS simulations are the largest suite of cDE simulations to date and are performed with a modified version (Baldi et al. 2010) of the widely used TreePM N-body code GADGET (Springel 2005). The code self-consistently simulates the evolution of structure formation in cDE models, taking into account the modified expansion history, the rise of a fifth force and additional friction on each particle and the time variation of the DM particle mass.

The set of CODECS simulations consists of two different types of runs, the L-CODECS and the H-CODECS runs. The H-CODECS simulations are adiabatic hydrodynamical simulations of a box of only 80 Mpc h^{-1} comoving describing the evolution of an equal number of DM and gas particles (512^3). As our focus is on larger scales, we instead exploit the L-CODECS runs, which follow the evolution of 1024^3 DM particles and as many baryons in a box of comoving side of 1 Gpc h^{-1}. Both DM and gas particles are treated as collisionless particles, but they experience different dynamics, as a consequence of the interaction between the CDM and the DE fluid. In fact, not properly taking into account the effect of the uncoupled baryonic fraction in interacting DE models would result in an incorrect evolution of structure formation. The run has a gravitational softening $\epsilon_s = 20$ kpc h^{-1} comoving; DM and baryon particles have a mass $m_{DM}(z = 0) = 5.84 \times 10^{10}$ M$_\odot$ h^{-1} and $m_b = 1.17 \times 10^{10}$ M$_\odot$ h^{-1}, respectively.

Six different cosmological models are simulated. The reference model is the standard ΛCDM model; three cDE models (EXP001, EXP002 and EXP003) are characterized by a constant positive coupling $\beta_c > 0$ and an exponential self-interaction potential of the form $V(\phi) = A\exp(-\alpha\phi)$. Another model (EXP008e3) has the same potential but an exponential coupling, $\beta_c(\phi) = \beta_0\exp(\beta_1\phi)$, and finally the last model (SUGRA003) has a constant negative coupling, $\beta_c < 0$, and a SUGRA (Brax & Martin 1999) self-interaction potential $V(\phi) = A\phi^{-\alpha}\exp(-\phi^2/2)$. We refer to table 2 in Baldi (2012b) for values of the potential parameters in each case.

The normalization of the models is consistent with the 7-year *Wilkinson Microwave Anisotropy Probe* (*WMAP*7) cosmology (Komatsu et al. 2011) and the linear matter power spectrum used to create initial conditions was computed with the publicly available code CAMB[3] (Lewis, Challinor & Lasenby 2000). All the models have the same amplitude of perturbations at $z = z_{CMB}$. Initial conditions

---

[3] www.camb.info

for the simulations have been created starting from a glass distribution (White [1994]; Baugh, Gaztanaga & Efstathiou [1995]) evaluating particle displacements at $z = 99$ using Zel'dovich approximation.

4 LENSING AND THE RAY-TRACING SIMULATIONS

4.1 The lensing observables

Because of the gravitational effects of matter on photons, light rays are deflected from their otherwise straight paths. The coherence scale of structures is negligible with respect to the cosmological distances involved in weak lensing studies, so it is reasonable to slice the matter distribution into thin shells using the well known *thin-lens* approximation. Under this hypothesis, cosmic lenses are effectively considered as two-dimensional objects whose projected mass distribution $\Sigma(\boldsymbol{\theta})$ on the lens plane is given by

$$\Sigma(\boldsymbol{\theta}) = \int \rho(\boldsymbol{\theta}, l)\, \mathrm{d}l, \tag{10}$$

where $\boldsymbol{\theta}$ is the angular position on the lens plane and l represents the direction along the line of sight.

The *convergence* is defined as

$$\kappa(\boldsymbol{\theta}) \equiv \frac{\Sigma(\boldsymbol{\theta})}{\Sigma_{\mathrm{crit}}}, \tag{11}$$

where Σ_{crit} represents the critical surface density and is defined as

$$\Sigma_{\mathrm{crit}} \equiv \frac{c^2}{4\pi G} \frac{D_{\mathrm{ds}}}{D_{\mathrm{d}} D_{\mathrm{s}}}, \tag{12}$$

where D_{ds}, D_{d} and D_{s} are the angular diameter distances between the lens and the source, between the observer and the lens and between the observer and the source, respectively. The ratio of the distances represents the lensing efficiency and its maximum value is for lensing approximately half way between the observer and the source.

Under the thin-shell approximation, the lens is fully described by its convergence and therefore through the two-dimensional Poisson equation by the lensing potential Ψ:

$$\nabla_{\boldsymbol{\theta}}^2 \Psi = 2\kappa(\boldsymbol{\theta}), \tag{13}$$

where the Laplacian is taken with respect to the angular position on the lens plane. The effect of the underlying matter distribution is to deflect the paths of light rays and it is possible to show that the bending angle $\hat{\alpha}$ is related to the lensing potential Ψ through

$$\hat{\alpha} = \nabla_{\boldsymbol{\theta}} \Psi. \tag{14}$$

As a consequence of the light deflection, the observed image of the sources gets distorted. The mapping between the original source shape and the actual observed image, up to second order, is given by (Goldberg & Bacon [2005]; Bacon et al. [2006])

$$\theta_i' \simeq A_{ij}\theta_j + \frac{1}{2} D_{ijk}\theta_j\theta_k. \tag{15}$$

In the previous equation, $A_{ij} \equiv \partial_j \theta_i'$ is the Jacobian matrix of the mapping between the lensed and unlensed images, θ_i' is the unlensed coordinate and the tensor D_{ijk} describing the mapping at second order is the derivative of the Jacobian matrix with respect to the lensed coordinates θ_i: $D_{ijk} \equiv \partial_k A_{ij}$. In the previous equations, $\partial_k \equiv \partial/\partial\theta_k$.

While the convergence κ gives a measure of the lensing strength weighted by the lens mass and the lensing efficiency, the distortions induced by gravitational lensing are quantified by the complex shear $\gamma = \gamma_1 + i\gamma_2$, which is related to the second derivatives of the lensing potential Ψ (Bartelmann & Schneider [2001]):

$$\gamma_1 = \frac{1}{2}(\partial_1^2 - \partial_2^2)\Psi, \tag{16}$$

$$\gamma_2 = \partial_{12}^2 \Psi. \tag{17}$$

The elements of the matrices A_{ij} and D_{ijk} are conveniently expressed as a function of the convergence, and of the shear components and its derivatives (see e.g. Goldberg & Bacon [2005]; Bacon et al. [2006]; Pace et al. [2011]). A suitable combination of the derivatives of the shear components gives rise to two new quantities, the one- and three-flexion (F and G, respectively; Bacon et al. [2006]):

$$F \equiv F_1 + iF_2 = (\gamma_{1,1} + \gamma_{2,2}) + i(\gamma_{2,1} - \gamma_{1,2}), \tag{18}$$

$$G \equiv G_1 + iG_2 = (\gamma_{1,1} - \gamma_{2,2}) + i(\gamma_{2,1} + \gamma_{1,2}). \tag{19}$$

The results derived so far are valid only in the case of a single lens between the observer and the source; however, the whole formalism can be generalized to the case of a continuous matter distribution. The procedure is very similar to the case of the single lens. The cosmic volume can be sliced in sufficiently small subvolumes whose thickness along the line of sight is sufficiently small with respect to the distances involved (namely the distances between the observer, the lenses and the sources). Therefore the thin-lens approximation should be valid and the matter distribution can be projected on a plane, and consequently the lensing potential can be evaluated using the Poisson equation. Also for multiple lenses therefore all the information is embedded in the lensing potentials on the slices. The final quantities (convergence, shear and flexion) can now be estimated on the source plane as the weighted sum of the contributions from all the different lensing planes. Unlike the single lens case, the Jacobian matrix is no longer symmetric, due to the fact that rotation of the light bundles can occur. As shown with the help of numerical simulations (see Jain, Seljak & White [2000]), the rotation term is very small and can be safely neglected; we verified that this is indeed the case for our simulations.

4.2 Ray-tracing simulations

Ray-tracing techniques consist of shooting rays through an *N*-body simulation and evaluating the deflection angle and related quantities by taking into account the underlying matter distribution.

The light cones are constructed by stacking snapshots of a single simulation; the snapshots are placed along the line of sight so that the light cone distance to the centre of the simulation corresponds with the time of the snapshot. We put sources at $z_{\mathrm{s}} = 1$ ($z_{\mathrm{s}} = 2$) using 10 (13) snapshots. Sufficient snapshots are stacked in order to avoid gaps in the matter distribution; this leads to some overlap in the stacking, which we account for by including only the volumes that do not overlap to the following snapshot in the stack.

Since each snapshot represents the same matter distribution at different cosmic times, the structures will be at roughly the same position in each volume. To avoid artificial correlations between the matter density at different redshifts, we coherently rotate and shift particle positions in each snapshot by a random amount, taking advantage of the periodic boundary conditions, so that particles leaving the simulated box on one side, re-enter on the opposite one. Finally, in order to estimate the sample variance errors, 100 different realizations were created for each model by using different shifts and rotations of the snapshots.

Table 1. Characteristic parameters for the ray-tracing simulations and normalization of the power spectrum.

Models	Opening angle ($^\circ$)	Resolution (arcsec)	Source comoving distance for $z_s = 1$ (Mpc h^{-1})	$\sigma_8 (z = 0)$
ΛCDM	24.34	21.39	2355.14	0.809
EXP001	24.36	21.41	2353.19	0.825
EXP002	24.39	21.44	2350.43	0.875
EXP003	24.43	21.47	2346.42	0.967
EXP008e3	24.55	21.58	2335.29	0.895
SUGRA003	25.23	22.17	2272.19	0.806

The opening angle of the ray-tracing simulation is evaluated with the comoving size and distance of the source plane. Because of a different background evolution, the distance of the source from the observer will slightly change with the model. For the reference ΛCDM model, the opening angle is $\theta = 24\overset{\circ}{.}34$ ($\theta = 15\overset{\circ}{.}4$) on a side and the resolution of the map is 21.39 (13.5) arcsec for sources at $z_s = 1$ ($z_s = 2$). In Table 1 we report these parameters for the other models considered in this paper. Although very similar, the map resolution is higher for the ΛCDM run since the sources are further away from the observer with respect to the other models. As seen in the second column of Table 1, the opening angle is minimum for the ΛCDM run and maximum for the SUGRA003 model. This is due to the fact that the opening angle is evaluated as the ratio of the comoving size of the source plane and its comoving distance with respect to the observer. (The comoving box size is the same for all the different models studied.) In the last column of Table 1 we present the normalization of the matter power spectrum for the different models. Note how the models have considerably different values of σ_8. In particular all the EXP models have a higher normalization with respect to the ΛCDM model, while for the SUGRA model it is approximately the same. As we will see later, this will have a crucial importance in explaining the differences between the models. All the models have the same amplitude of scalar perturbations at z_{CMB}, therefore, the different normalizations at $z = 0$ reflect the different structure evolution, as shown by the growth factor in fig. 2 of Baldi (2012b). All the EXP models show a monotonic increase of the ratio of the linear growth factor with respect to the ΛCDM model, while the SUGRA model recovers the amplitude of perturbations at $z = 0$.

We next briefly sketch how we created the lensing maps. For more details we refer the reader to Hamana & Mellier (2001) and Pace et al. (2007, 2011). For each lens plane (which corresponds roughly to the snapshots), we evaluate the projected matter density field and then with fast Fourier transform (FFT) techniques we can recover the corresponding lensing potential. The selected particles are projected parallel to the line of sight on a two dimensional grid of 4096^2 pixels; to assign particles to pixels, we use the triangular-shape-cloud (TSC) method as outlined in Hockney & Eastwood (1988). Following the prescription of Hamana & Mellier (2001), we project particles over a regular grid to obtain the projected overdensity field for each lens plane:

$$\delta_{ij}^{\text{proj},k} = \frac{M_{ij}^k}{A_k \bar{\rho}_k} - L_k, \tag{20}$$

where the index k runs over the lens planes, M_{ij}^k is the mass projected in the box k on the pixel (ij), A_k the pixel area and L_k the size of the projected box (in our case it will be smaller than the full box size, due to the overlapping volumes). Finally, $\bar{\rho}_k$ is the comoving background density. Note that $\bar{\rho}(a) = \bar{\rho}_0 \Omega_0$ only for the ΛCDM model, since for other models the time evolution of the matter density parameter is different from the standard $(1 + z)^3$ behaviour.

Formally the lensing potential is still evaluated via the two-dimensional Poisson equation, but in this case we also have to take into account the different matter density parameter evolution. We therefore write the Poisson equation as (Hamana & Mellier 2001)

$$\nabla_x^2 \Psi^k = \frac{8\pi G \bar{\rho}_k}{c^2} \delta^{\text{proj},k}. \tag{21}$$

Equation (21) can be solved via FFT techniques taking advantage of the periodic boundary conditions. As shown above (see Section 4.1), the lensing potential fully characterizes our system. We can therefore obtain all the lensing quantities we are interested in via standard finite difference techniques.

The ray-tracing simulations are based on stacking multiple lensing planes and the result evaluated on the source plane is given by adding the weighted contribution of all the planes between the source and the observer. Suppose the cosmic volume is sliced into N lens planes and the source plane is labelled as $N + 1$. Light rays are shot from the observer and create a regular grid on the first lens plane. The bend angle on a given plane k is related to the image position $\boldsymbol{\theta}_1$ on the first lens plane ($N = 1$) through the relation

$$\boldsymbol{\theta}_k = \boldsymbol{\theta}_1 - \sum_{i=1}^{k-1} \frac{f_K(w_k - w_i)}{f_K(w_k) a_i} \nabla_x \Psi_i(\boldsymbol{x}), \tag{22}$$

where w is the comoving distance, a_i the scale factor of the lens plane, f_K a function depending on the cosmology and $\Psi_i(\boldsymbol{x})$ the Newtonian potential projected along the line of sight on each lens plane.

The Jacobian on each lens plane is obtained by differentiating equation (22) with respect to $\boldsymbol{\theta}_1$. By defining $\mathbf{A}_k \equiv \partial \boldsymbol{\theta}_k / \partial \boldsymbol{\theta}_1$ and indicating with $\mathbf{U}_k$ the matrix whose elements are the second derivatives of the lensing potential we derive the following equation:

$$\mathbf{A}_k = \mathbf{I} - \sum_{i=1}^{k-1} \frac{f_K(w_i) f_K(w_k - w_i)}{f_K(w_k) a_i} U_i A_i, \tag{23}$$

where $\mathbf{I}$ represents the identity matrix. A further derivative of equation (23) with respect to $\boldsymbol{\theta}_i$ gives a similar recursive relation for the two flexions (Pace et al. 2007, 2011):

$$\mathbf{D}_k^{1,2} = - \sum_{i=1}^{k-1} \frac{f_K(w_i) f_K(w_k - w_i)}{f_K(w_k) a_i} [f_K w_i G_U^{1,2} + U_i D_i^{1,2}]. \tag{24}$$

In the previous equation, $G_U \equiv \nabla_x U$ is a tensor containing the third derivatives of the lensing potential.

On the source plane, the matrices $\mathbf{A}$ and $\mathbf{D}^{1,2}$ can be related to observable quantities like the effective convergence, shear and derivatives of the shear (that combined together provide the one- and three-flexion). They read

$$\mathbf{A}_{N+1} = \begin{pmatrix} 1 - \kappa - \gamma_1 & -\gamma_2 + \omega \\ -\gamma_2 - \omega & 1 - \kappa + \gamma_1 \end{pmatrix},$$

$$\mathbf{D}_{N+1}^1 = \begin{pmatrix} -2\gamma_{1,1} - \gamma_{2,2} & -\gamma_{2,1} + \omega_1 \\ -\gamma_{2,1} + \omega_2 & -\gamma_{2,2} + \omega_3 \end{pmatrix},$$

$$\mathbf{D}_{N+1}^2 = \begin{pmatrix} -\gamma_{2,1} + \omega_4 & -\gamma_{2,2} + \omega_5 \\ -\gamma_{2,2} + \omega_6 & 2\gamma_{1,2} - \gamma_{2,1} \end{pmatrix}. \quad (25)$$

The scalar ω is called the rotation term and describes the rotation of the light bundle due to multiple lenses. Following Bacon & Schäfer (2009), we identify the additional quantities ω_i, with $i = 1$–6, as a combination of the components of the twist $C \equiv C_1 + \iota C_2$ and the turn $T = T_1 + \iota T_2$:

$$\omega_1 = -\frac{1}{2}(C_1 + T_1 + T_2), \quad (26)$$

$$\omega_2 = -\frac{1}{2}(C_1 + T_1 - T_2), \quad (27)$$

$$\omega_3 = T_1 + T_2, \quad (28)$$

$$\omega_4 = T_1 - T_2, \quad (29)$$

$$\omega_5 = \frac{1}{2}(C_1 - T_1 - T_2), \quad (30)$$

$$\omega_6 = -\frac{1}{2}(C_2 + T_1 + T_2). \quad (31)$$

We performed several tests on our ray-tracing simulations and showed that our results are largely unaffected by their presence, so we neglect them below.

As an example, in Fig. 1 we show one realization of the effective convergence maps. For all the models we used the same random seed so to have the same distribution of structures along the light cone. As expected, the main pattern of the effective convergence κ is very similar for all the models, but some differences can be noticed even by eye. In particular we observe that the realization for the SUGRA003 model, despite having basically the same normalization of the ΛCDM model, shows less pronounced structures and lower convergence peaks. The EXP003 model, on the other hand, presents a larger number of structures and higher peaks, due to the higher normalization of the matter power spectrum. Similar conclusions can be drawn for the other models, where differences become more evident when the matter power spectrum normalization increases.

In the following sections these differences, already visible by eye, will be analysed in a more quantitative way using various statistical tests and will be explained in terms of the different evolution of the matter density perturbations in the various cosmological models.

5 RESULTS

In this section we describe the results we obtained from the analysis of our simulated maps. In Section 5.1 we discuss results related to the lensing power spectrum and in Sections 5.2 and 5.3 the shear in aperture and the correlation function, respectively. In Section 5.4 we illustrate results regarding the probability distribution function (PDF) of some of the lensing quantities. In Section 5.5 we examine higher order moments such as the variance, the skewness and the kurtosis. All results shown in this section are the average (or median) values computed over 100 different realizations, while the error bars (shown only for the reference ΛCDM model for clarity reasons) represent the rms (or quartiles) of the same 100 realizations.

5.1 Power spectrum

We begin with the study of the power spectra of different lensing observables in the simulated maps. The shear (or effective convergence) power spectrum is a very important observational quantity that can be used to probe the underlying cosmological model, to infer the normalization of the matter power spectrum and the growth of structures. In the Born approximation, the shear power spectrum is related to the integral along the line of sight of the matter power spectrum, weighted by distance factors taking into account the geometry of the system (in particular the relative distances between source, lens and observer). As explained before, in cDE models, DM evolution no longer follows the a^{-3} time evolution, and the time evolution of the power spectrum is affected by this. The relation between the matter $P_\delta(k)$ and the lensing $P_\kappa(\ell)$ power spectra is given by (see also Beynon et al. 2012)

$$P_\kappa(\ell) = \frac{9}{4}\left(\frac{H_0}{c}\right)^4 \int_0^{\chi_H} d\chi\, W^2(\chi) f(a) P_\delta\left(k = \frac{\ell}{\chi}, \chi\right), \quad (32)$$

where $f(a) = a^4 \Omega_m^2(a) E^4(a)$, $E \equiv H/H_0$ is the dimensionless Hubble function, χ_H the comoving distance to the horizon and $\Omega_m(a)$ the matter density evaluated at the scale factor a.

In the weak lensing regime (the one of interest for this work), the spectra of shear γ, reduced shear g, convergence κ and flexions F and G are all interrelated; in particular

$$P_\gamma(\ell) = P_\kappa(\ell) = P_g(\ell), \quad (33)$$

$$P_F(\ell) = P_G(\ell) = \ell^2 P_\kappa(\ell). \quad (34)$$

In reality the true observable is the power spectrum of the reduced shear g, defined as

$$g \equiv \frac{\gamma}{1 - \kappa}, \quad (35)$$

and its spectrum is approximately the same as the one for cosmic shear, as distortions of the images are very small.

To evaluate the power spectrum of the different lensing quantities we consider each pixelated map and evaluate its Fourier transform on the grid. We then multiply each map in Fourier space by its complex conjugate and determine the corresponding frequency at each pixel. A further binning of the spectrum obtained in this way gives the final smoothed result.

In Fig. 2 we show the ratio between the lensing power spectrum of the cDE models and the reference spectrum of the ΛCDM model. Since the power spectrum for the (reduced) shear is identical to that of the effective convergence and the spectra of the two flexions are simple functions of the convergence, we limit ourself to the ratios for the effective convergence. We show our results for wavelengths up to $\ell \approx 2 \times 10^4$, since for higher values, the noise in our simulations starts dominating. The model EXP001 has a slightly different σ_8 and differences are of the order of few per cent; it is well within the error bars at all the wavelengths probed in our ray-tracing simulations, making it very difficult to distinguish it from the reference model. It is similarly difficult to discriminate between the SUGRA003 model and the ΛCDM model on large scales, since the ratio is well within the simulation uncertainty from cosmic variance. The largest deviations appear for the model EXP003 where on large scales the differences are around 40 per cent.

In the EXP models the power is higher than for the ΛCDM model: this is due to the faster growth of perturbations and therefore to higher matter power spectrum normalization; this is reflected directly in the different amplitude at small ℓ. The SUGRA003 model
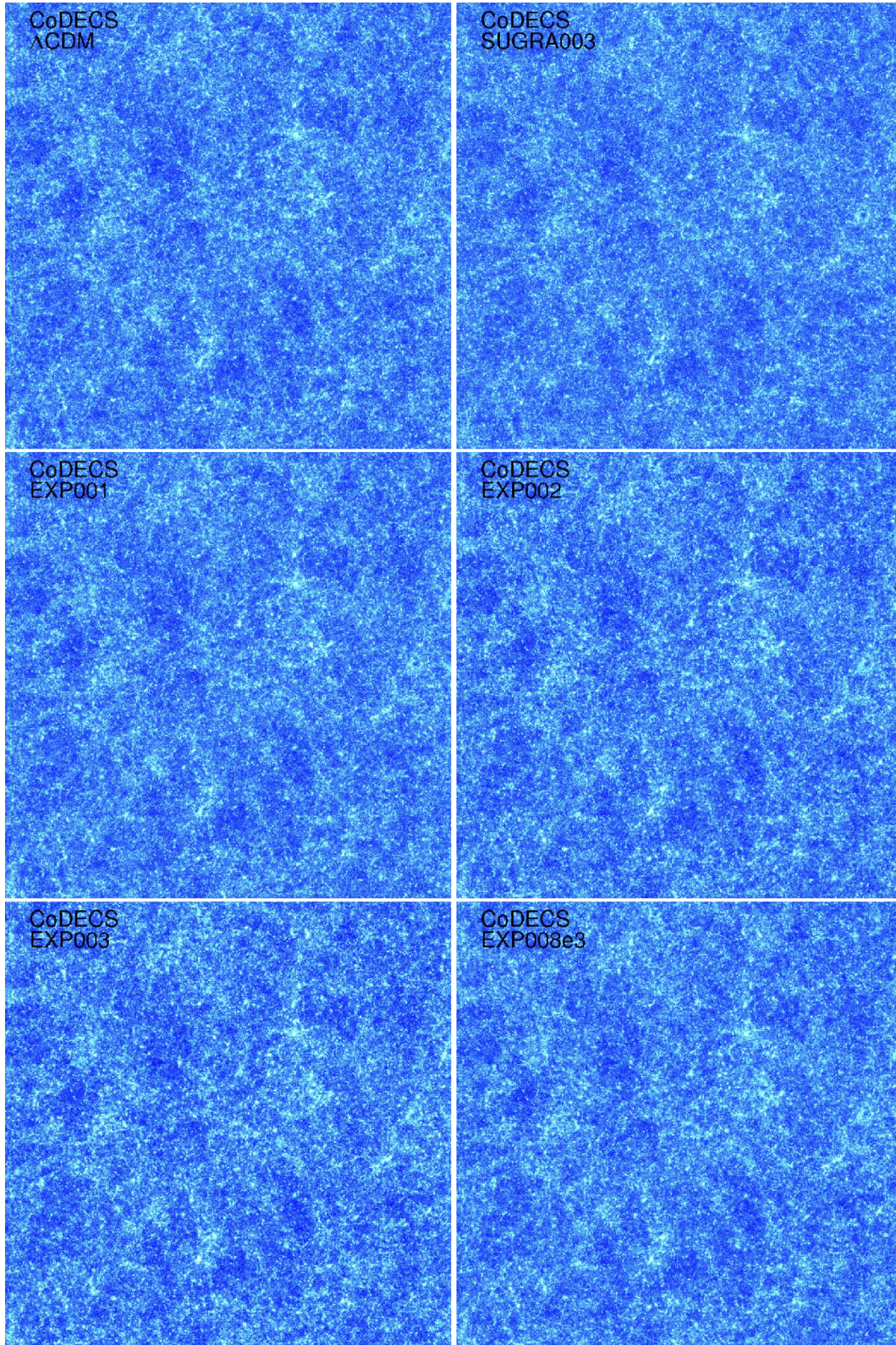
Figure 1. The effective convergence for one particular realization of the ray-tracing simulations used in this work. Sources are at $z_s = 1$. Colour range is the same for all the models. Different panels refer to different cosmological models, as labelled. We refer to Table 1 for the field of view spanned by each simulation.
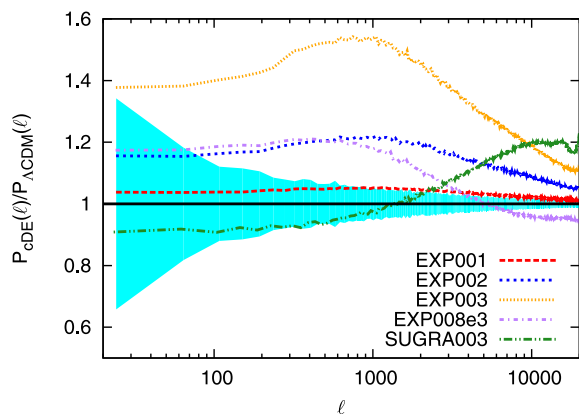
Figure 2. Ratio between the convergence power spectrum of the cDE models and the reference ΛCDM model as a function of the multipole ℓ. Different colours and line styles represent different models. The ΛCDM model is shown with solid black line, the EXP001 model with dashed red line, the EXP002 model with blue short-dashed line, the EXP003 model with orange dotted line, the EXP008e3 model with the light violet dashed–dotted line and finally the SUGRA003 model with the green dashed-dot-dotted line. The curves and the shaded region (shown only for the ΛCDM model) represent the average and the rms obtained from 100 different realizations, respectively.

Figure 3. Ratio between the convergence power spectrum of the EXP003 (orange dotted line) and the reference ΛCDM model. For comparison we show the same ratio obtained analytically for a ΛCDM model having the same normalization $\sigma_8 = 0.967$ as the EXP003 model (black thin solid line).

is quite different. Despite having basically the same σ_8 normalization as the ΛCDM model, we notice approximately 10 per cent less power up to $\ell \approx 1000$. This is easily explained in terms of the evolution of the matter density parameter, which for the SUGRA003 model is consistently smaller than that of the ΛCDM model at the redshifts of interest for this work. This is due to the evolution of the DM mass. As shown in equation (32), the lensing power spectrum is proportional to the matter density parameter, therefore, a deficit in this quantity will directly translate into a lower power spectrum. These conclusions follow closely and reproduce the results on the matter power spectrum presented in Baldi (2012b) also in the weak lensing regime.

It is also interesting to notice an increase in the power with a peak at $\ell \approx 1000$, followed by a later decrease in the region dominated by the shot noise (an increase for the SUGRA003 model). These results, including the increase in the ratio, are in good qualitative agreement with Carbone et al. (2013), though that work probed a much smaller range of multipoles than in this work. It is worth understanding whether the differences that arise are purely due to the different growth rate and power spectrum normalization, or reflect deeper physical differences in the models. To address this question, we evaluate analytically the lensing power spectrum for a ΛCDM model with the same normalization $\sigma_8 = 0.967$ as the EXP003 model and we show our results in Fig. 3. On large scales, we observe a fairly good agreement between the EXP003 model and the ΛCDM model with higher power spectrum normalization. (The lack of power for the largest modes is due to the missing power in the simulations arising from its finite size.) The increase of power we observe for the cDE model at higher multipoles also appears in this case, so it is evidently simply the result of the different normalization. This is consistent with the different σ_8; although the amplitude is lower, it is in agreement with what was found for the three-dimensional matter power spectrum in Baldi (2012b). The peak originates from the different evolution of the non-linear matter power spectrum; in particular, models with a higher normalization will have non-linear effects kicking in at lower ℓs with respect to a model with a lower normalization. The feature occurs precisely
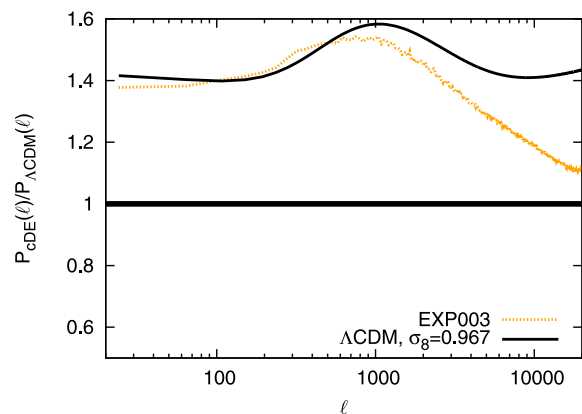
at the linear-non-linear transition scale for the model with higher normalization (at the redshift being probed.)

However, the normalization is not the only effect at play; at higher ℓs, the EXP003 spectrum drops away from the analytical ΛCDM spectrum and the agreement is limited up to $\ell \approx 1000$. At the largest multipoles, we do not expect agreement between the analytic and simulations due to the finite resolution of the pixels in the ray-traced maps (see also Pace et al. 2007, 2011). Comparing analytic and simulated ΛCDM spectra, these effects are seen to suppress the spectra above $\ell \approx 4000$, and so below this any suppressions we see in the cDE models are believed to result from the modified physics. In order to examine the impacts at higher resolutions, we focus our attention on ratios of simulations where the pixel smoothing effects should cancel. Note that these smoothing effects equally impact the shear in aperture (Section 5.2) and the PDF (Section 5.4) observables.

While there is consensus that the reduced shear is the truly observable shear quantity, for flexion several possibilities have been considered. Viola, Melchior & Bartelmann (2012) defined the reduced flexions in analogy to the reduced shear:

$$\mathcal{F} = \frac{F}{1-\kappa}, \tag{36}$$

$$\mathcal{G} = \frac{G}{1-\kappa}, \tag{37}$$

while Schneider & Er (2008) instead studied

$$\mathcal{F} = \frac{F + gF^*}{1-\kappa}, \tag{38}$$

$$\mathcal{G} = \frac{G + gF}{1-\kappa}, \tag{39}$$

where F^* represents the complex conjugate of F. We have created reduced flexion maps according to both definitions and find that the results are very similar. In particular, ratios between the spectra of the reduced flexions for the cDE models and the ΛCDM model are equivalent to what is found for the unreduced flexion.

It is well known that it is possible to gain information on the time evolution of the large-scale structure of the Universe by following a tomographic approach, i.e. studying the lensing effects produced on sources located at different redshifts. To investigate this issue in the context of cDE models, we have also used a set of effective

convergence maps created for sources at $z_s = 2$, and we have evaluated for each model the ratio of the power spectra for sources at $z_s = 2$ and the ones for sources at $z_s = 1$. The aim is to see whether there is any signature due to the coupling that would make the ratio dependent on the multipoles in a peculiar way. We find that this is unfortunately not the case, since all the ratios are very similar to what is found for the ΛCDM model. Small differences are seen at very high ℓ, where unfortunately we cannot completely trust our results due to the increase of noise and to resolution effects. Therefore the study of the convergence power spectrum with sources at different redshifts seems not to add any further information to what is inferred from the analysis at $z_s = 1$. This is due to the combination of the evolution of the DM parameter and friction terms.

We have seen that the ratios between the convergence power spectra of the different models faithfully reproduce the behaviour of the matter power spectrum, as explained in detail in Baldi (2012b). In particular the EXP (SUGRA) models show a higher (lower) spectrum amplitude. There will also be degeneracies between the EXP and the ΛCDM model with respect to different values of σ_8 and between the SUGRA and the ΛCDM model with respect to different values for the matter density parameter Ω_m. To investigate these degeneracies, it would be necessary to run a larger suite of N-body simulations covering an array of models. This is beyond the scope of the present work, where we focus on the study of the effects of the coupling between DM and DE on the lensing observables.

5.2 Shear in aperture

An alternative statistic to the power spectrum is the shear in aperture. The shear in aperture represents the variance of the shear field within a circular aperture of radius θ and it is related to the power spectrum by

$$|\gamma_{av}(\theta)|^2 \equiv 2\pi \int_0^\infty d\ell\, \ell P_\gamma(\ell) \left[\frac{J_1(\ell\theta)}{\pi\ell\theta} \right]^2, \qquad (40)$$

where $J_1(x)$ is the first-order Bessel function of the first kind.

In Fig. 4 we show our results for the shear in aperture as a function of the angular scale θ. In the upper panel we show a comparison between the values of the shear in aperture for the ΛCDM model (black solid line) and the two most extreme cDE models, the EXP003 model (orange dotted line) and the SUGRA003 model (green dashed-dot-dotted line). The power spectrum differences between the models translate to differences in the shear in aperture, but in an integrated, cumulative way.

For smaller apertures, the finite resolution of the simulations also becomes an issue, as can be seen by comparing with analytical predictions for the ΛCDM model (black dashed line). From Fig. 4, we see that simulations reliably reproduce the expected analytical result only for angles $\theta \geq 2$ arcmin, while on smaller scales the differences become substantial. For scales of the order of 0.3 arcmin, the lack of signal is about ≈ 30 per cent. Our plot is very similar to that shown in Bartelmann & Schneider (2001), their fig. 19. The deficit is similar to what happens when the linear spectrum is used instead of the non-linear one. While our simulation is obviously fully non-linear, due to resolution effects, we lose some of the power on non-linear scales.

In the lower panel of Fig. 4, we show the ratio of the cDE models with respect to the reference model. Again, the shaded region represents the error bars obtained as rms of 100 different realizations. Error bars increase with increasing angular scale, since there are fewer independent patches in the map to average over. Since the simulation scatter is very small (shaded region), the EXP003
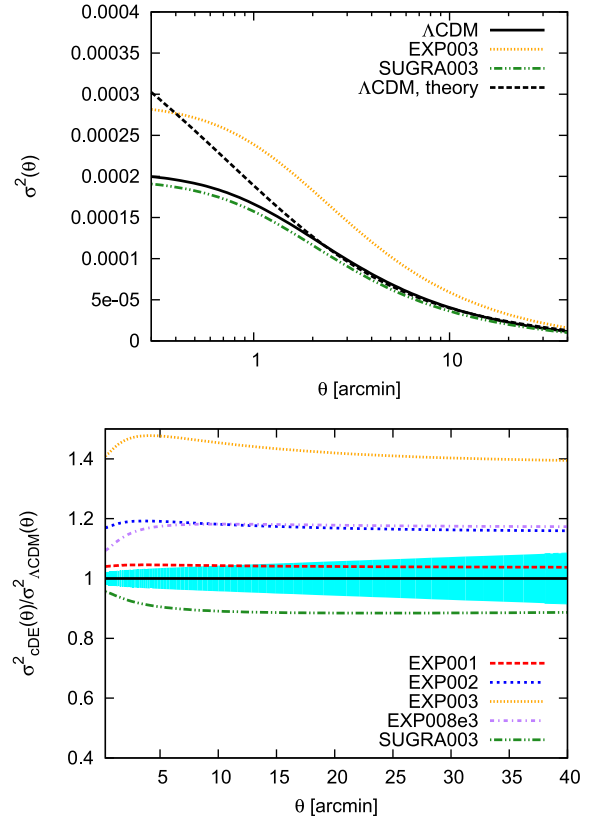

Figure 4. Shear in aperture. Upper panel: the results for the reference ΛCDM model and for the two most extreme cDE models (SUGRA003 and EXP003). For comparison we also show the analytical prediction for the ΛCDM model (dashed black line). Lower panel: the ratio between the cDE models and the ΛCDM model. Colour lines and styles are as in Fig. 2. The curves and the shaded region (shown only for the ΛCDM model) represent the average and the rms obtained from 100 different realizations, respectively.

model could be easily distinguished from the ΛCDM model given such an observation. In general, the ratios have similar values to the ones found for the lensing power spectrum, and the ratio is approximately constant over the range of angular scales investigated in this work. Once again the different behaviour of the models is easily interpreted in terms of the different normalization of the matter power spectra (EXP models) and of the time evolution of the matter density parameter (the SUGRA003 model).

The reason why the ratio is approximately constant on all scales relates to the definition of the shear in aperture (equation 40). As noticed in Section 5.1, the spectra are approximately a rescaled version of the ΛCDM model, therefore, also its integral over the multipoles will be such that the variance is approximately a rescaled version of the ΛCDM expression. This is indeed confirmed in Fig. 4.

As in Section 5.1, we wish to see whether the differences in the shear in aperture predictions are simply due to the higher normalization or we can observe some feature more directly reflecting the new physics. We again compared the EXP003 model with the predictions for a ΛCDM model having identical matter power spectrum normalization. Such a comparison shows a qualitative agreement on the ratios with respect to the reference ΛCDM model, including the peak in the ratio for $\theta \approx$ few arcmin. There is also a smaller impact from the feature seen in the power spectrum ratios, as we verified with a control ratio of the shear in aperture for two ΛCDM models with different matter power spectrum normalization. Nevertheless,

the amplitude of the EXP003 model is lower than the amplitude of the ΛCDM model with analogous normalization of the matter power spectrum. This is in agreement with our finding for the convergence power spectrum (see Fig. 3) and it is due to the friction term in the equations of motion. We refer to Baldi (2012b) for a further discussion of the subject.

5.3 Shear correlation function

Another counterpart of the lensing power spectrum discussed in Section 5.1 is the shear correlation function defined as

$$\xi_+(\theta) = \int_0^\infty \mathrm{d}\ell \frac{\ell}{2\pi} P_\kappa(\ell) J_0(\ell\theta), \tag{41}$$

where $J_0(x)$ is the Bessel function of order zero, $P_\kappa(\ell)$ the effective convergence power spectrum and θ the angular distance between the correlated sources. Note that the kernel in the integrand is different from the shear in aperture statistics, therefore, these can be compared only qualitatively.

A detailed study of the shear correlation function was performed by Beynon et al. (2012), which we refer to for more details. However, there is a substantial difference compared to that work: our simulations assume that all the sources are at $z_s = 1$, while in Beynon et al. (2012) sources follow a different redshift distribution according to the different weak lensing survey the prediction is made for. Moreover their shear correlation function is presented only for the models EXP001, EXP002 and EXP003. We can therefore only make a qualitative comparison between the two different analyses.

We present the correlation functions in Fig. 5 as a function of the angular scale θ. In the upper panel we show a comparison between the values of the shear correlation function for the ΛCDM model (black solid line) and the two most extreme cDE models, the EXP003 model (orange dotted line) and the SUGRA003 model (green dashed-dot-dotted line). As expected, with respect to the reference ΛCDM model, we see an excess (a lack) of correlation for the EXP003 (SUGRA003) model. Once again, we can explain this result in terms of the different matter density evolution (SUGRA003 model) and of the different matter power spectrum normalization (EXP003 model).

In the lower panel of Fig. 5, we present the differences of the shear correlation function $\xi_+(\theta)$ between the cDE models and the ΛCDM model. The shaded region represents the 1σ error bar as obtained averaging over 100 realizations. In agreement with Beynon et al. (2012), we see that errors decrease with increasing the correlation angle. This is expected since there are more objects to average over. The amplitude of the rms errors is different from Beynon et al. (2012), since ours is based on the different realizations performed, while the value presented in Beynon et al. (2012) refers to the discriminatory power of the specific survey.

With respect to Beynon et al. (2012), our predictions for the shear correlation function are somewhat higher. This is expected since in our simulations all the sources are at the same redshift. The differences in the shear correlation functions arising from different redshift distributions of the sources are not a simple constant, but it is a function of the angular scale. In addition, the behaviour at small angular scales is due to resolution effects that lead to a loss of power.

To summarize, our results are in good qualitative agreement with Beynon et al. (2012). Models with higher power spectrum normalization show a higher amplitude of the shear correlation function while the SUGRA model presents a deficit in the signal (since we
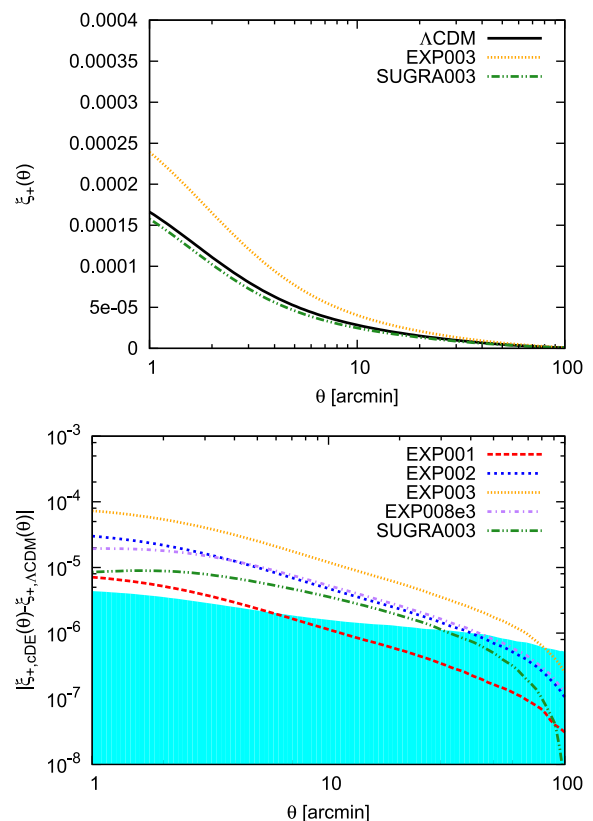

Figure 5. Shear correlation function. Upper panel: the results for the reference ΛCDM model and for the two most extreme cDE models (SUGRA003 and EXP003). Lower panel: absolute value of the difference between the cDE models and the ΛCDM model. Colour lines and styles are as in Fig. 2. The curves and the shaded region (shown only for the ΛCDM model) represent the average and the rms obtained from 100 different realizations, respectively.

take the absolute values, the SUGRA model lies above the EXP001 model). The trend closely follows what found for the study of the power spectrum and of the shear in aperture. The model EXP001 is once again barely above the 1σ error bars, making it therefore difficult to detect (differently from what found in Beynon et al. 2012), but on a wide range of angular scales the EXP003 will be clearly identified. Models EXP002 and EXP008e3 behave in a very similar way, analogously to what found for the power spectrum and shear in aperture. All the other models are within the error bars for $\theta \gtrsim 30$–40 arcmin, once again differently from Beynon et al. (2012). Taking into account that as shown in fig. 5 of Beynon et al. (2012), using HALOFIT (Smith et al. 2003) introduces errors of the same order of magnitude of the intrinsic differences between the models, we can conclude that ray-tracing simulations are an important tool in studying this class of models.

5.4 Probability distribution function

While the power spectrum and shear in aperture fundamentally reflect the same statistical information, it is interesting to explore whether non-Gaussianity of the lensing statistics can help distinguish between the different physics. We explore this first by examining the full one-point PDF, and discuss moments of the PDF in the next section. We limit our discussion to quantities that can be effectively observed, in particular to the effective convergence, the

(modulus of the) shear, one- and three-flexion (*F* and *G*) and finally the magnification.

To infer the PDF from our simulated lensing maps, we first establish the absolute minimum and maximum of the maps for a given quantity, then we bin the values of the maps in this interval. Since each map has a different range of values, binning the pixels in a range enclosed by the absolute minima and maxima allows us to compute the ratio between the different models straightforwardly, without the need to interpolate or extrapolate the numerical PDF.

As it is apparent from Fig. 6, for the modulus of the shear and of the two flexions, differences between the cDE models and the ΛCDM model are of the order of 20–40 per cent, and percentage differences for the two flexions are similar to those for shear. In particular the model EXP003 now shows differences of the order of 40 per cent with respect to the ΛCDM model. We notice that error bars are relatively small for all the quantities, but at the two extremes representing relatively rare extreme underdense and overdense regions. As seen above, the models most significantly different from the reference one are the SUGRA003 and the EXP003, due to the lower effective matter density parameter for the first and the higher matter power spectrum normalization for the second. The shear PDF instead is more sensitive to the matter power spectrum normalization; we see that differences can be up to 40 per cent and approximately constant over a few decades of the shear values.

Regarding the effective convergence, we see in the top panel of Fig. 6 that differences between the models grow largest in the high convergence tail. Note that unlike the shear and flexion moduli, the convergence can take both positive and negative values and it can be well fitted by a lognormal distribution with mean $\kappa_0 = 0.04$ and variance $\sigma = 0.35$ (following the notation of Taruya et al. 2002; Hilbert, Hartlap & Schneider 2011). For models with an increasing power spectrum normalization, differences become more pronounced, particularly for the most extreme EXP003 model, which is characterized by a very high σ_8. The models SUGRA003 and EXP008e3 are quite interesting; having a slightly lower normalization than the ΛCDM model, the SUGRA003 model has an excess of high convergence points. On the other hand, the EXP008e3 model, despite having a significantly higher normalization, shows no change in the tail with respect to the fiducial model. These demonstrate that the friction terms can have a very pronounced effect on the formation of non-linear structures. This was also seen in small-scale power spectrum in Fig. 2.

While gravitational lensing preserves the surface brightness, this is not the case for the apparent solid angle of a source. The magnification μ, defined as the ratio of the image area to the source area, can be expressed in terms of the shear γ and effective convergence κ via the relation

$$\mu = \frac{1}{(1-\kappa)^2 - \gamma^2}. \tag{42}$$

Recently the magnification has become an active research field for cosmology due to its power in complementing shear studies (Bernstein & Jarvis 2002; van Waerbeke 2010; Van Waerbeke et al. 2010; Hildebrandt et al. 2011, 2013; Ford et al. 2012; Casaponsa et al. 2013; Heavens, Alsing & Jaffe 2013).

Examining Fig. 7, we notice that magnification can also be an excellent discriminant between different models, even if in this case error bars are much bigger than before at the high magnification tail. In particular, as noticed with the effective convergence case, the model EXP003, having a much higher σ_8, makes a higher magnification of the source more probable. This is easily understood by considering the relation between the magnification and the

effective convergence, $\mu \simeq 1 + 2\kappa$ (valid at first order) when both the shear and the effective convergence are small. Therefore higher values of the convergence also imply higher values for the magnification. At second order, taking into account both the effective convergence and the shear, the relation between the magnification and these two quantities becomes (Ménard et al. 2003; Takahashi et al. 2011; Marra, Quartin & Amendola 2013)

$$\mu \simeq 1 + 2\kappa + 3\kappa^2 + \gamma^2 + \mathcal{O}(\kappa^3, \gamma^3). \tag{43}$$

The magnification μ, up to second order, depends on the convergence κ and its square (κ^2) and on the square of the modulus of the shear (γ^2). In Fig. 6 we saw that both the effective convergence and the shear are sensitive to the background cosmological model; therefore, we cannot neglect the contribution coming from the shear. While at small shear and convergence we can relate the two PDFs via the expression (Takahashi et al. 2011)

$$\frac{\mathrm{d}P_\mu}{\mathrm{d}\mu} = \frac{(1-\kappa)^3}{2} \frac{\mathrm{d}P_\kappa}{\mathrm{d}\kappa}, \tag{44}$$

where $\mathrm{d}P_\mu/\mathrm{d}\mu$ and $\mathrm{d}P_\kappa/\mathrm{d}\kappa$ are the PDF's of the magnification and of the effective convergence, respectively, this is no longer accurate at larger values of convergence and shear. This is reflected in comparing the top panels of Fig. 6 with Fig. 7.

As for the power spectrum, it is interesting to understand which PDF differences are simply due to the different normalization of the models and which are more intrinsic. To evaluate the PDF of the effective convergence or of the shear, two different approaches have been followed in the literature. On one hand, perturbation theory techniques (see e.g. Munshi & Jain 2000; Valageas 2000a,b; Taruya et al. 2002; Ménard et al. 2003; Valageas, Barber & Munshi 2004; Valageas & Munshi 2004; Takahashi et al. 2011) and the halo model (Takada & Hamana 2003) were exploited to analytically infer the PDF of the effective convergence κ, the modulus of γ and of the magnification μ; on the other hand, with the help of *N*-body simulations, numerical fits to the PDF of the effective convergence were determined, so as to have a quick recipe when cosmological parameters have to be changed, for example the matter density $\Omega_{\mathrm{m},0}$ and the matter power spectrum normalization σ_8 (see e.g. Hilbert et al. 2011; Marra et al. 2013).

For this work we use the output of the TURBOGL code[4] (Kainulainen & Marra 2009, 2011). The TURBOGL code is based on the stochastic approach to cumulative weak lensing and on generating stochastic configurations of haloes along the line of sight, or along the photon geodesic from the source to the observer. Haloes that model virialized structures are described by a Navarro–Frenk–White density profile (Navarro et al. 1996; Navarro, Frenk & White 1997), filaments as non-uniform cylindrical objects. In addition, the modelling takes into account the fact that most of the cosmic volume is occupied by voids while most of the mass is in virialized structures and filaments. We show the comparison for the PDF of the effective convergence and of the magnification in Fig. 8 with different normalization of the matter power spectrum for the ΛCDM and EXP003 model.

It is apparent that the differences between the EXP003 and the ΛCDM model can be entirely explained in terms of the different normalization of the matter power spectrum. The range we can use is however limited, due to the fact that the ray-tracing procedure underestimates the true PDF for the effective convergence and magnification: this is due to the limited pixel resolution and mass

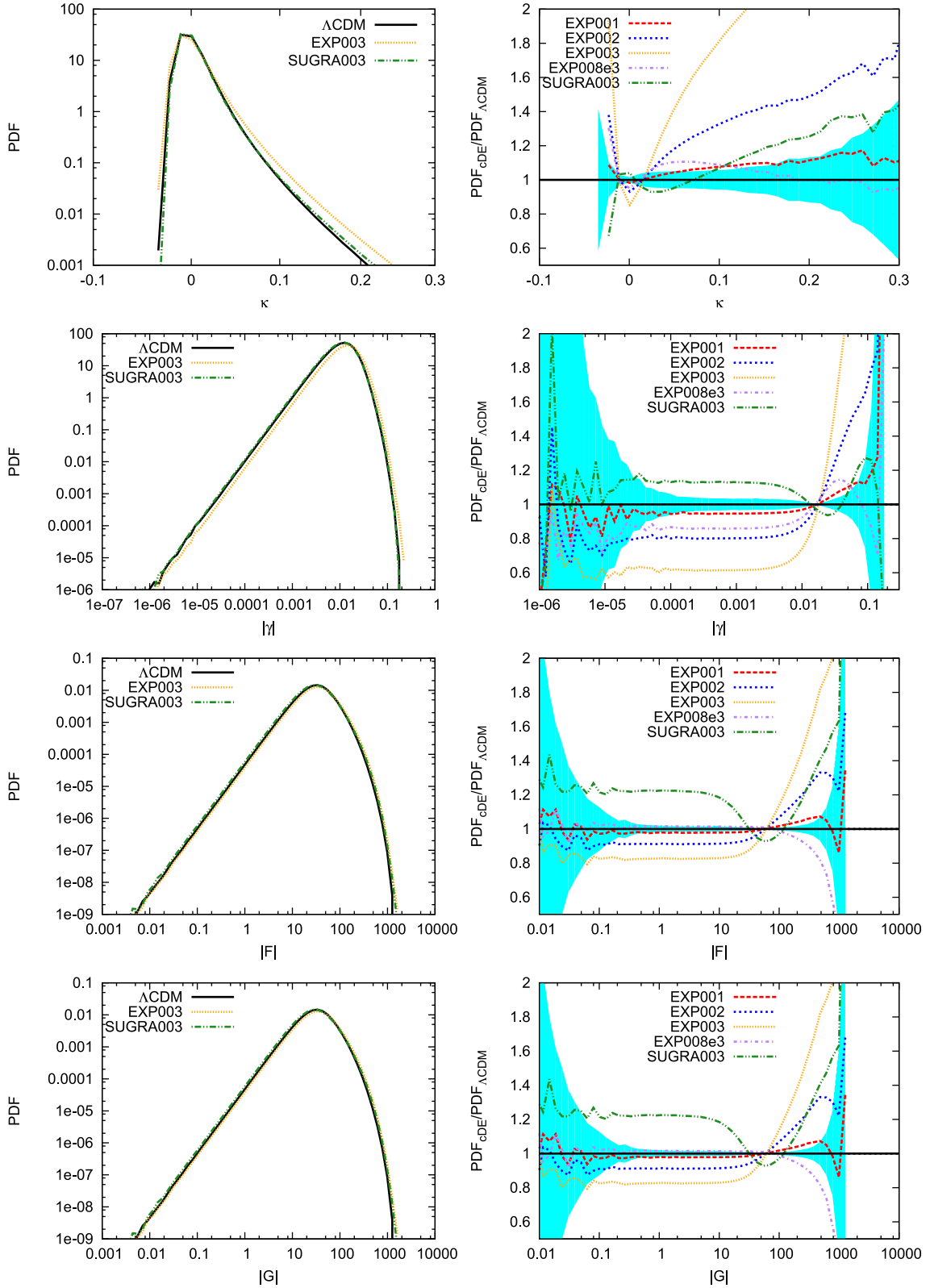---

[4] http://www.turbogl.org/

Figure 6. PDF for several lensing quantities analysed in this work. From top to bottom: effective convergence κ, modulus of the shear γ, one- and three-flexion (F and G, respectively). Left-hand panels show the results for the reference ΛCDM model and for the two most extreme cDE models (SUGRA003 and EXP003). Right-hand panels show the ratio between the cDE models and the ΛCDM model. Colour lines and styles are as in Fig. 2. The curves and the shaded region (shown only for ΛCDM model) represent the average and the rms obtained from 100 different realizations, respectively.
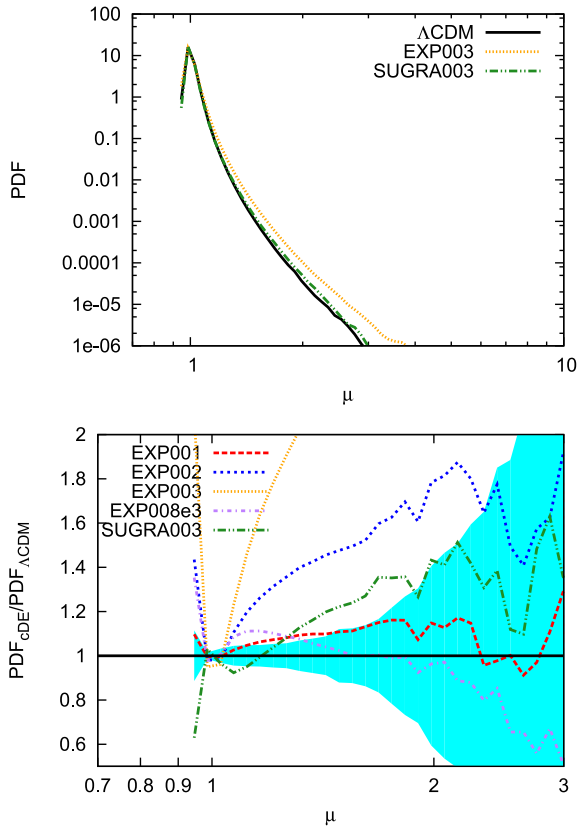
Figure 7. PDF for the cosmic magnification. The upper panel shows the results for the reference ΛCDM model and for the two most extreme cDE models (SUGRA003 and EXP003). The lower panel shows the ratio between the cDE models and the ΛCDM model. Colour lines and styles are as in Fig. 2. The curves and the shaded region (shown only for ΛCDM model) represent the average and the rms obtained from 100 different realizations, respectively.
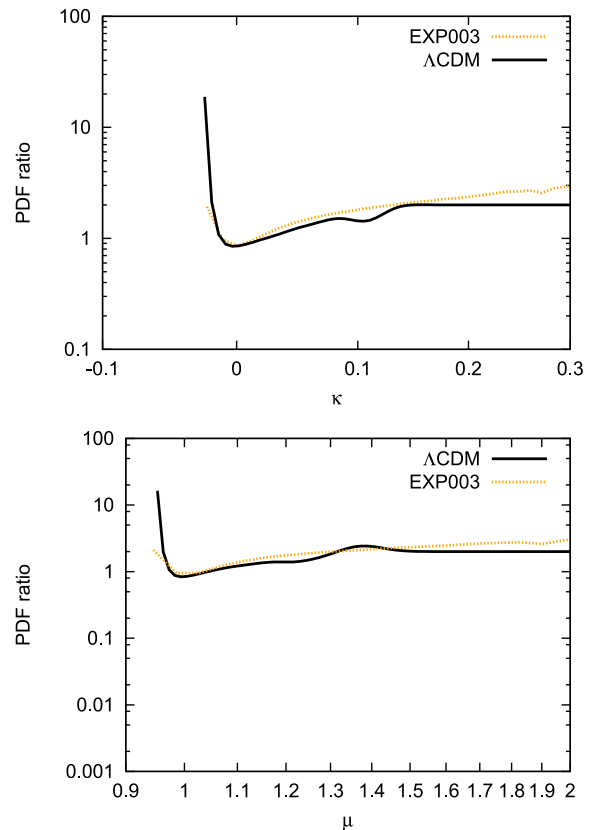

Figure 8. Ratio between the PDF of the EXP003 (orange dotted line) and the reference ΛCDM model. For comparison we show the same ratio obtained with the TURBOGL code for a ΛCDM model having the same normalization $\sigma_8 = 0.967$ as the EXP003 model (black solid line). The upper and lower panels refer to the effective convergence κ and to the magnification μ, respectively.

assignment to create the lens planes (Killedar et al. 2012). In addition, the tail of the two distributions are not very well sampled, therefore, we cannot draw any conclusion on the fact that for high values of the effective convergence (and hence magnification), the two curves show small differences.

5.5 Mean, median, variance, skewness and kurtosis

Signatures of coupling between DE and DM can be more easily quantified by considering higher order moments of the PDF. The PDF (Section 5.4) represents the one-point distribution, while the power spectrum (Section 5.1) and the shear in aperture (Section 5.2) represent second-order moments.

Next we will focus on the mean, the median, the variance, the skewness and the kurtosis of the PDF of the effective convergence, and by considering these at varying resolutions we effectively include the effect of spatial correlations.

Unfortunately, these statistical quantities are often affected by large errors which make their use on real data more difficult.

The mean μ_1, the variance μ_2, the skewness μ_3 and the kurtosis μ_4 are defined as

$$\mu_1 = \frac{1}{N^2} \sum_{ij} \kappa_{i,j}, \qquad (45)$$

$$\mu_2 = \frac{1}{N^2} \sum_{ij} \left(\kappa_{i,j} - \bar{\kappa} \right)^2, \qquad (46)$$

$$\mu_3 = \frac{\mu_2^{-3/2}}{N^2} \sum_{ij} \left(\kappa_{i,j} - \bar{\kappa} \right)^3, \qquad (47)$$

$$\mu_4 = \frac{\mu_2^{-2}}{N^2} \sum_{ij} \left(\kappa_{i,j} - \bar{\kappa} \right)^4 - 3, \qquad (48)$$

where $\bar{\kappa} \equiv \mu_1$ is the mean value of the effective convergence. To evaluate the different moments of the convergence maps, we subtract the mean value $\bar{\kappa}$ from the maps, and divide by the total number of pixels N^2 to get the appropriate normalization.

Since the distribution of the convergence is non-Gaussian and its mean is effectively zero, it is useful to consider the median, $\mu_{1/2}$, i.e. the value at which the integrated probability is the same above and below. In Fig. 9, we show the median, the variance, the skewness and the kurtosis as a function of the map resolution. To do so, we binned our high-resolution convergence maps to progressively decrease the number of pixels in the maps, and, as consequence, to make the map resolution progressively worse. Working with sources at $z_s = 1$, we created new sets of maps, with 2048^2, 1024^2, 512^2, 256^2 and 128^2 pixels. The corresponding resolutions are
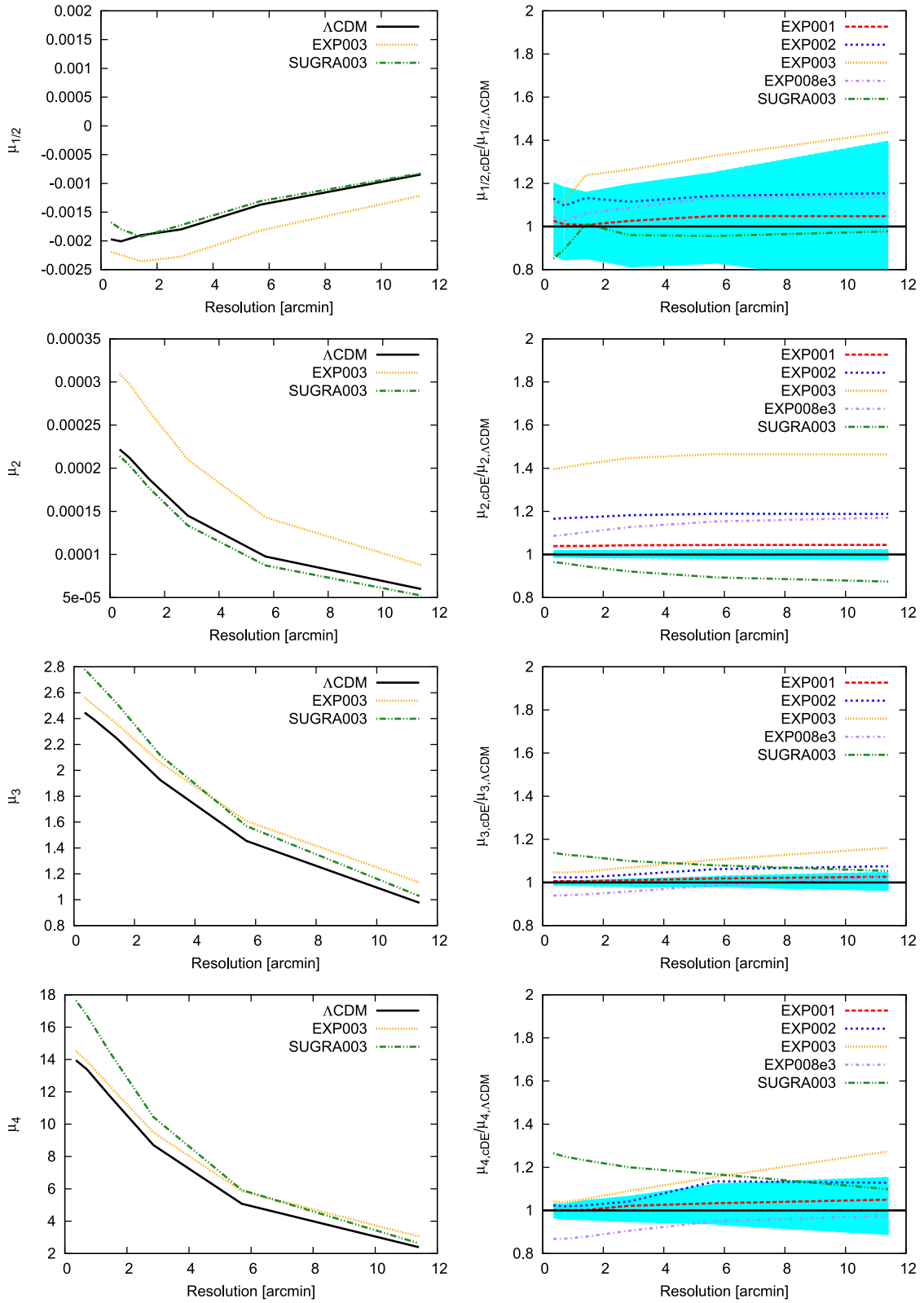
Figure 9. From top to bottom: median of the distribution for the median ($\mu_{1/2}$), variance (μ_2), skewness (μ_3) and kurtosis (μ_4) of the effective convergence field as a function of the pixel resolution scale. Left-hand panels show the results for the reference ΛCDM model and for the two most extreme cDE models (SUGRA003 and EXP003). Right-hand panels show the ratio between the cDE models and the ΛCDM model. Colour lines and styles are as in Fig. 2. The curves and the shaded region (shown only for ΛCDM model) represent the median and the quartiles obtained from 100 different realizations, respectively.
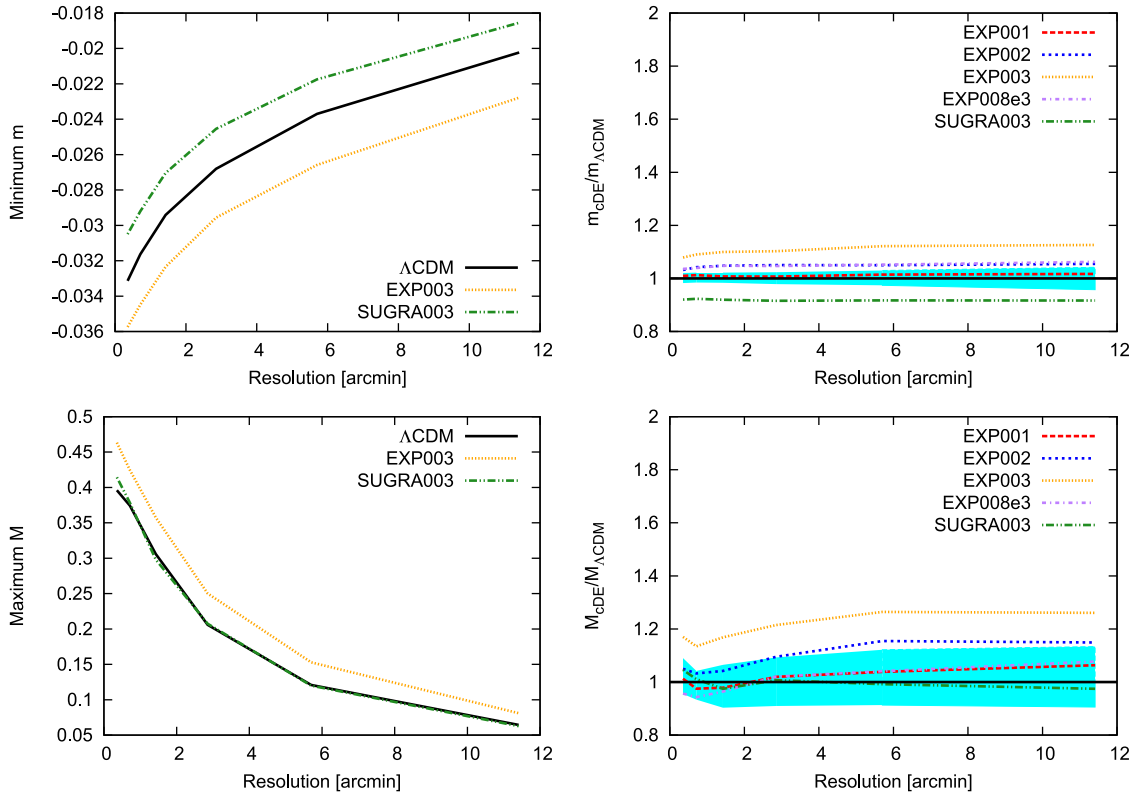
Figure 10. Upper (lower) panels: median of the distribution of minima *m* (maxima *M*) as a function of the map resolution scale. Left-hand panels show the results for the reference ΛCDM model and for the two most extreme cDE models (SUGRA003 and EXP003). Right-hand panels show the ratio between the cDE models and the ΛCDM model. Colour lines and styles are as in Fig. 2. The curves and the shaded region (shown only for ΛCDM model) represent the median and the quartiles obtained from 100 different realizations, respectively.

(for a ΛCDM model), from 4096^2 to 128^2 pixels, 0.356, 0.71, 1.4, 2.9, 5.7 and 11.4 arcmin, respectively.

For each quantity we show its median value and the shaded region represents the range between the first and the third quartiles of the set of points for the ΛCDM simulation. Thus it envelopes the central 50 per cent of the distribution, as opposed to the 1σ regions shown previously.

As expected, the variance shows a very similar behaviour to the convergence power spectrum and shear in aperture, also from a quantitative point of view. All the EXP models show higher values for the variance, while the expected value for the SUGRA003 model is ≈12 per cent lower than the ΛCDM model. The EXP001 is just outside of the quartile area, making therefore difficult to distinguish it at a 1σ level. Other models instead show progressively higher differences. As expected, increasing the order of the moments makes the quartiles increase, to the point that all the models will be indistinguishable from the reference one. In particular, while for the variance only the EXP001 model is comparable with the quartiles, for the skewness only the EXP003 model is more than 1σ away than the ΛCDM model, and for the kurtosis all the models are basically within the error bars. At high resolution the skewness has the potential of distinguishing between the different models, but its predictive power decreases at lower resolutions.

In the case of the median, the area enclosed by the quartiles is rather large, making this statistical quantity largely insensitive to the background model, with the exception once again of the EXP003 model. While the median changes by a factor of 2 over the resolution scale analysed in this work, we see that the ratio is approximately constant.

We conclude therefore that only the variance can be used as a discriminant between the different models, since for higher order statistics, error bars overcome the inner differences between the models. A further comment has to be made regarding the error bars and the possibility of using higher order moments of the effective convergence. Error bars and quartiles represent effectively the variance between the maps, each of them covering an area of roughly 600 deg^2. Therefore our conclusions and the possibility of using the skewness and the kurtosis for lensing studies are limited to surveys of this size. Larger surveys will have reduced errors bars and higher order moments could be used as useful cosmological probes.

Finally, we investigate whether the most extreme behaviour, namely the maximum or minimum value in the entire map, might be a good discriminant of the models. In Fig. 10 we present the median of the maxima (*M*) and of the minima (*m*) for the ensemble of effective convergence maps. As expected, these are moderate when the resolution decreases and more pixels are averaged together. These highlight the asymmetry of the distributions, as the minima are significantly smaller in magnitude compared to the maxima. However, the differences between models are quite limited for the minima, at most 10–15 per cent with larger differences for the SUGRA003 and EXP003 models. In particular the SUGRA003 (EXP003) model shows less (more) pronounced minima with respect to the ΛCDM model and this can be explained with the different matter density evolution (normalization of the matter power spectrum). Maxima instead show a clear trend with normalization of the matter power spectrum: the higher σ_8, the higher are the differences (up to ≈20 per cent). It is also worth noting that the distribution of the maxima is very sensitive to the map resolution: while minima change

only by a factor of 1.7, maxima change by a factor of 10. As these are rare events, the intrinsic scatter is large, making these a poor discriminator of models.

6 CONCLUSIONS

In this work we have studied weak lensing statistics of cDE models (Baldi 2012b), characterized by an interaction between the DM and the DE. Our aim was to extend previous work on the subject (see Beynon et al. 2012; Carbone et al. 2013), going beyond the Born approximation with full ray-tracing simulations to provide a realistic simulated suite for lensing quantities, in particular effective convergence, shear, flexions and magnification. The advantage of the numerical approach is that full non-linearity is automatically achieved and no approximation is necessary for a full analysis (which is usually required with analytical techniques).

A coupling between DM and DE has important effects on structure formation due to the different non-linear evolution of DM particles, and the appearance of a fifth force term that, because of its frictional nature, tends to suppress non-linear power.

We saw that all the statistical quantities analysed in this work faithfully reproduce features observed in the study of the three-dimensional matter distribution. In particular, we observe the following.

(i) The effective convergence (shear) power spectrum faithfully reproduces results from Baldi (2012b) regarding the three-dimensional matter power spectrum. Differences on large scales can be explained by the different normalization of the matter power spectrum, but a comparison with a ΛCDM model having the same normalization of the matter power spectrum reveals the importance of the different non-linear evolution, showing a suppression of power at small scales. Differences for the cDE model characterized by a SUGRA potential can be explained by the different evolution of the matter density parameter.

(ii) PDFs are sensitive to the different background models and could be used to discriminate between the different cDE models. We showed that differences between the models can be mainly explained by differences in the normalization of the matter power spectrum, but the high convergence tail can signal differences in the non-linear evolution arising from friction terms.

(iii) When evaluating the moments of the effective convergence, we find that only the variance can be used as a statistical tool to infer the background cosmological model. Higher order statistics like the skewness and the kurtosis are more prone to sample variability between the different realizations, making them less sensitive for discriminating between the different models.

Our simulations have assumed that all the sources are at a fixed redshift, in order to make ray-tracing simulations numerically less expensive. The errors we infer are limited by the finite size of the simulations, and would correspond to a moderate sized survey of order 600 deg^2, significantly smaller than ongoing or future surveys such as DES or *Euclid*. Our primary aim has been to study whether in principle other weak lensing statistics can provide a useful probe to models of cDE; at the same time, we have developed techniques that will be required to take into account non-linear effects in weak lensing.

To conclude, differences on large scales between the cDE models and the ΛCDM model can largely be explained by the modified growth rate and DM fraction, leading to different normalization of the matter power spectrum. On small scales where non-linear effects

kick in, a suppression of power is caused by friction terms which lead to observable signatures in the power spectrum and the PDF.

REFERENCES

Allen S. W., Schmidt R. W., Ebeling H., Fabian A. C., van Speybroeck L., 2004, MNRAS, 353, 457
Allen S. W., Rapetti D. A., Schmidt R. W., Ebeling H., Morris R. G., Fabian A. C., 2008, MNRAS, 383, 879
Amendola L., 2000, Phys. Rev. D, 62, 043511
Amendola L., 2004, Phys. Rev. D, 69, 103524
Amendola L., Campos G. C., Rosenfeld R., 2007, Phys. Rev. D, 75, 083506
Amendola L., Baldi M., Wetterich C., 2008, Phys. Rev. D, 78, 023015
Amendola L. et al., 2013, Living Rev. Relativ., 16, 6
Astier P., Pain R., 2012, Comptes Rendus – Phys., 13, 521
Astier P. et al., 2006, A&A, 447, 31
Bacon D. J., Schäfer B. M., 2009, MNRAS, 396, 2167
Bacon D. J., Goldberg D. M., Rowe B. T. P., Taylor A. N., 2006, MNRAS, 365, 414
Baldi M., 2011a, MNRAS, 411, 1077
Baldi M., 2011b, MNRAS, 414, 116
Baldi M., 2012a, MNRAS, 420, 430
Baldi M., 2012b, MNRAS, 422, 1028
Baldi M., Salucci P., 2012, J. Cosmol. Astropart. Phys., 2, 14
Baldi M., Pettorino V., Robbers G., Springel V., 2010, MNRAS, 403, 1684
Baldi M., Pettorino V., Amendola L., Wetterich C., 2011, MNRAS, 418, 214
Bartelmann M., 2010, Rev. Modern Phys., 82, 331
Bartelmann M., Schneider P., 2001, Phys. Rep., 340, 291
Baugh C. M., Gaztanaga E., Efstathiou G., 1995, MNRAS, 274, 1049
Bean R., Flanagan É. É., Laszlo I., Trodden M., 2008, Phys. Rev. D, 78, 123514
Benson B. A. et al., 2013, ApJ, 763, 147
Bernstein G. M., Jarvis M., 2002, AJ, 123, 583
Bertone G., Hooper D., Silk J., 2005, Phys. Rep., 405, 279
Beynon E., Baldi M., Bacon D. J., Koyama K., Sabiu C., 2012, MNRAS, 422, 3546
Blake C. et al., 2012, MNRAS, 425, 405
Böhmer C. G., Caldera-Cabral G., Chan N., Lazkoz R., Maartens R., 2010, Phys. Rev. D, 81, 083003
Boylan-Kolchin M., Bullock J. S., Kaplinghat M., 2011, MNRAS, 415, L40
Brax P. H., Martin J., 1999, Phys. Lett. B, 468, 40
Caldera-Cabral G., Maartens R., Ureña-López L. A., 2009a, Phys. Rev. D, 79, 063518
Caldera-Cabral G., Maartens R., Schaefer B. M., 2009b, J. Cosmol. Astropart. Phys., 7, 27
Carbone C., Baldi M., Pettorino V., Baccigalupi C., 2013, J. Cosmol. Astropart. Phys., 9, 4

Casaponsa B., Heavens A. F., Kitching T. D., Miller L., Barreiro R. B., Martínez-González E., 2013, MNRAS, 430, 2844

Cervantes V. D. V., Marulli F., Moscardini L., Baldi M., Cimatti A., 2012, preprint (arXiv:1212.0853)

Clemson T., Koyama K., Zhao G.-B., Maartens R., Väliviita J., 2012, Phys. Rev. D, 85, 043007

Cole S. et al., 2005, MNRAS, 362, 505

Conley A. et al., 2011, ApJS, 192, 1

Cui W., Baldi M., Borgani S., 2012, MNRAS, 424, 993

de la Torre S. et al., 2013, A&A, 557, A54

di Porto C., Amendola L., 2008, Phys. Rev. D, 77, 083508

Eisenstein D. J. et al., 2005, ApJ, 633, 560

Ettori S., 2003, MNRAS, 344, L13

Ford J. et al., 2012, ApJ, 754, 143

Fu L. et al., 2008, A&A, 479, 9

Giannantonio T., Scranton R., Crittenden R. G., Nichol R. C., Boughn S. P., Myers A. D., Richards G. T., 2008, Phys. Rev. D, 77, 123520

Goldberg D. M., Bacon D. J., 2005, ApJ, 619, 741

Guzzo L. et al., 2008, Nature, 451, 541

Hagiwara K. et al., 2002, Phys. Rev. D, 66, 010001

Haiman Z., Mohr J. J., Holder G. P., 2001, ApJ, 553, 545

Hamana T., Mellier Y., 2001, MNRAS, 327, 169

Heavens A., Alsing J., Jaffe A. H., 2013, MNRAS, 433, L6

Hilbert S., Hartlap J., Schneider P., 2011, A&A, 536, A85

Hildebrandt H. et al., 2011, ApJ, 733, L30

Hildebrandt H. et al., 2013, MNRAS, 429, 3230

Hinshaw G. et al., 2013, ApJS, 208, 19

Ho S., Hirata C., Padmanabhan N., Seljak U., Bahcall N., 2008, Phys. Rev. D, 78, 043519

Hockney R. W., Eastwood J. W., 1988, Computer Simulation Using Particles. Hilger, Bristol

Hoekstra H. et al., 2006, ApJ, 647, 116

Jaffe A. H. et al., 2001, Phys. Rev. Lett., 86, 3475

Jain B., Seljak U., White S., 2000, ApJ, 530, 547

Jarosik N. et al., 2011, ApJS, 192, 14

Jarvis M., Jain B., Bernstein G., Dolney D., 2006, ApJ, 644, 71

Kainulainen K., Marra V., 2009, Phys. Rev. D, 80, 123020

Kainulainen K., Marra V., 2011, Phys. Rev. D, 83, 023009

Kessler R. et al., 2009, ApJS, 185, 32

Kilbinger M. et al., 2013, MNRAS, 430, 2200

Killedar M., Lasky P. D., Lewis G. F., Fluke C. J., 2012, MNRAS, 420, 155

Komatsu E. et al., 2011, ApJS, 192, 18

Kowalski M. et al., 2008, ApJ, 686, 749

Koyama K., Maartens R., Song Y.-S., 2009, J. Cosmol. Astropart. Phys., 10, 17

Laureijs R. et al., 2011, preprint (arXiv:1110.3193)

La Vacca G., Kristiansen J. R., Colombo L. P. L., Mainini R., Bonometto S. A., 2009, J. Cosmol. Astropart. Phys., 4, 7

Lee J., Baldi M., 2012, ApJ, 747, 45

Lewis A., Challinor A., Lasenby A., 2000, ApJ, 538, 473

Li B., 2011, MNRAS, 411, 2615

Li B., Barrow J. D., 2011a, Phys. Rev. D, 83, 024007

Li B., Barrow J. D., 2011b, MNRAS, 413, 262

Lopez Honorez L., Reid B. A., Mena O., Verde L., Jimenez R., 2010, J. Cosmol. Astropart. Phys., 9, 29

McCarthy I. G., Bower R. G., Balogh M. L., 2007, MNRAS, 377, 1457

Macciò A. V., Quercellini C., Mainini R., Amendola L., Bonometto S. A., 2004, Phys. Rev. D, 69, 123516

Majerotto E., Väliviita J., Maartens R., 2010, MNRAS, 402, 2344

Mantz A., Allen S. W., Rapetti D., Ebeling H., 2010, MNRAS, 406, 1759

Marra V., Quartin M., Amendola L., 2013, Phys. Rev. D, 88, 063004

Marulli F., Baldi M., Moscardini L., 2012, MNRAS, 420, 2377

Ménard B., Hamana T., Bartelmann M., Yoshida N., 2003, A&A, 403, 817

Munshi D., Jain B., 2000, MNRAS, 318, 109

Navarro J. F., Frenk C. S., White S. D. M., 1996, ApJ, 462, 563

Navarro J. F., Frenk C. S., White S. D. M., 1997, ApJ, 490, 493

Pace F., Maturi M., Meneghetti M., Bartelmann M., Moscardini L., Dolag K., 2007, A&A, 471, 731

Pace F., Moscardini L., Bartelmann M., Branchini E., Dolag K., Grossi M., Matarrese S., 2011, MNRAS, 411, 595

Parkinson D. et al., 2012, Phys. Rev. D, 86, 103518

Percival W. J. et al., 2001, MNRAS, 327, 1297

Percival W. J. et al., 2010, MNRAS, 401, 2148

Perlmutter S. et al., 1999, ApJ, 517, 565

Pettorino V., Baccigalupi C., 2008, Phys. Rev. D, 77, 103003

Planck Collaboration XV, 2014a, A&A, 571, A15

Planck Collaboration XVI, 2014b, A&A, 571, A16

Planck Collaboration, 2014c, A&A, 571, A19

Rapetti D., Allen S. W., Mantz A., Ebeling H., 2010, MNRAS, 406, 1796

Reid B. A. et al., 2010, MNRAS, 404, 60

Riess A. G. et al., 1998, AJ, 116, 1009

Riess A. G. et al., 2004, ApJ, 607, 665

Rozo E. et al., 2010, ApJ, 708, 645

Sahni V., Starobinsky A., 2000, Int. J. Modern Phys. D, 9, 373

Sánchez A. G. et al., 2014, MNRAS, 440, 2692

Schmidt B. P. et al., 1998, ApJ, 507, 46

Schneider P., Er X., 2008, A&A, 485, 363

Schrabback T. et al., 2010, A&A, 516, A63

Sherwin B. D. et al., 2011, Phys. Rev. Lett., 107, 021302

Smith R. E. et al., 2003, MNRAS, 341, 1311

Springel V., 2005, MNRAS, 364, 1105

Sullivan M. et al., 2011, ApJ, 737, 102

Takada M., Hamana T., 2003, MNRAS, 346, 949

Takahashi R., Oguri M., Sato M., Hamana T., 2011, ApJ, 742, 15

Taruya A., Takada M., Hamana T., Kayo I., Futamase T., 2002, ApJ, 571, 638

Tegmark M. et al., 2004, Phys. Rev. D, 69, 103501

Valageas P., 2000a, A&A, 354, 767

Valageas P., 2000b, A&A, 356, 771

Valageas P., Munshi D., 2004, MNRAS, 354, 1146

Valageas P., Barber A. J., Munshi D., 2004, MNRAS, 347, 654

Väliviita J., Maartens R., Majerotto E., 2010, MNRAS, 402, 2355

van Waerbeke L., 2010, MNRAS, 401, 2093

Van Waerbeke L., Hildebrandt H., Ford J., Milkeraitis M., 2010, ApJ, 723, L13

Veropalumbo A., Marulli F., Moscardini L., Moresco M., Cimatti A., 2014, MNRAS, 442, 3275

Vikhlinin A. et al., 2009, ApJ, 692, 1060

Viola M., Melchior P., Bartelmann M., 2012, MNRAS, 419, 2215

Wang S., Khoury J., Haiman Z., May M., 2004, Phys. Rev. D, 70, 123008

Watkins R., Feldman H. A., Hudson M. J., 2009, MNRAS, 392, 743

Weinberg S., 1989, Rev. Modern Phys., 61, 1

Wetterich C., 1995, A&A, 301, 321

White S. D. M., 1994, preprint (arXiv:astro-ph/9410043)

Xia J.-Q., 2009, Phys. Rev. D, 80, 103514

Zlatev I., Wang L., Steinhardt P. J., 1999, Phys. Rev. Lett., 82, 896

This paper has been typeset from a TEX/LATEX file prepared by the author.